# Controlling swelling in mixed transport polymers through alkyl side-chain physical cross-linking

Nicholas Siemons[a,b] (ID), Drew Pearce[a], Hang Yu[a], Sachetan M. Tuladhar[a], Garrett S. LeCroy[b], Rajendar Sheelamanthula[c] (ID), Rawad K. Hallani[c], Alberto Salleo[b], Iain McCulloch[c], Alexander Giovannitti[b,d], Jarvist M. Frost[e] (ID), and Jenny Nelson[a,1] (ID)

Semiconducting conjugated polymers bearing glycol side chains can simultaneously transport both electronic and ionic charges with high charge mobilities, making them ideal electrode materials for a range of bioelectronic devices. However, heavily glycolated conjugated polymer films have been observed to swell irreversibly when subjected to an electrochemical bias in an aqueous electrolyte. The excessive swelling can lead to the degradation of their microstructure, and subsequently reduced device performance. An effective strategy to control polymer film swelling is to copolymerize glycolated repeat units with a fraction of monomers bearing alkyl side chains, although the microscopic mechanism that constrains swelling is unknown. Here we investigate, experimentally and computationally, a series of archetypal mixed transporting copolymers with varying ratios of glycolated and alkylated repeat units. Experimentally we observe that exchanging 10% of the glycol side chains for alkyl leads to significantly reduced film swelling and an increase in electrochemical stability. Through molecular dynamics simulation of the amorphous phase of the materials, we observe the formation of polymer networks mediated by alkyl side-chain interactions. When in the presence of water, the network becomes increasingly connected, counteracting the volumetric expansion of the polymer film.

conjugated polymers | organic electrochemical devices | soft materials | structure-property relationships | mixed electronic-ionic conductors

Conjugated polymers functionalized with ethylene glycol side chains can transport both electronic and ionic charges ("mixed transport") when paired with liquid electrolytes. Especially when paired with aqueous electrolytes, mixed transport polymers have demonstrated wide applicability in bioelectronic devices such as biosensors (1), organic electrochemical transistors (OECTs) (2–4), batteries, and supercapacitors (5). During the operation of, for example, an energy storage device, a bias is applied across the mixed transport polymer electrodes causing electronic charges to form on their backbones (electrons on the cathode and holes on the anode). Simultaneously, ions and their solvation shells penetrate into the electrodes to compensate for the injected electronic charges, causing the electrodes to swell. Polymers with glycol side chains have been reported to swell excessively with aqueous electrolytes, leading to detrimental changes to the microstructure and poor device stability (6–8). Alterations to the chemistry of the side chains, for example changing the side-chain lengths (7, 8), using amphiphilic side chains (9, 10) and copolymerizing alkylated and glycolated repeat units (3, 11) have been shown to impact the degree to which the materials swell. Using polymers with both alkyl and glycol side chains has emerged as a popular strategy (12, 13), in part due to reports that exchanging a small fraction of glycol side chains for alkyl side chains can reduce the swelling of the polymer medium substantially (3, 11). As well as impacting the degree to which mixed transport polymers swell, side-chain engineering can influence how the polymers pack (14, 15), interact with electrolyte (14, 16, 17) and how they behave during photocatalytic charge transfer processes (18–20).

However, other than the notion that introducing apolar chemical groups reduces the swelling of the polymer medium, little is known about how copolymerizing glycolated polymers with alkylated repeat units alters the polymer film microstructure, and therefore about the mechanism by which the swelling is inhibited. Experimental characterizations are hindered predominantly for two reasons; first, swelling characteristics depend on many factors (level of crystallinity, local morphology, batch-to-batch differences, etc.), which can lead to nonmonotonic swelling trends with the alkyl content of the polymer (21). Second, experimental characterizations of the microstructure, for example through diffraction-based techniques, primarily explore the crystalline phase, with the effect of alkyl side chains on the microstructure being difficult to determine. For example, some reports comparing alkylated and glycolated polymers show that alkyl side chains result in

## Significance

Side-chain engineering has been repeatedly demonstrated as an effective strategy for optimizing the physical properties of organic mixed ionic and electronic transporting polymers, enabling the design of a range of electrochemical devices. However, the mechanisms through which side-chain engineering affects macroscopic properties of mixed transport polymers are not well understood. Using both molecular modeling and experiment, we find that detrimental swelling of these mixed transport materials can be controlled through the formation of supramolecular networks mediated by alkyl side chains in the bulk of the polymer. These findings could assist the rational design of high-performance and resilient polymer materials for future electrochemical devices.

smaller pi-stacking distances (21), some indicate they increase the pi-stacking distances (4, 22, 23), and others indicate they have no effect (24).

While levels of crystallinity play an important role in water uptake (25), the majority of the films' volume is amorphous and most of the water enters the amorphous phase during swelling (25, 26). The difficulty of gaining insight into the amorphous microstructure of the polymer films is perhaps the biggest impediment in understanding the impact of exchanging glycol side chains for alkyl side chains. Molecular Dynamics (MD) modeling is a useful technique for studying structure and dynamics of mixed transport polymers. MD has, for example, demonstrated the solid-gel switching behavior of a typical mixed transporting polythiophene, p(gT2) (6), and shown that electronic charge transport pathways are disrupted in mixed transport polymer films upon inclusion of alkyl side chains (27).

However, MD is not without its challenges. MD typically allows access to nanosecond time scales with a few hundred thousand atoms, while many processes in mixed transport polymer systems happen on longer times scales and involve many more atoms. Using MD to model swelling, in particular, is challenging since swelling can occur on time scales of up to minutes and can be highly anisotropic (26). In standard MD, it is not possible to access these time or length scales, but trends in properties such as swelling rates can be simulated and compared between the materials.

Furthermore, the statistical significance of an observation made from MD can be difficult to quantify (28). One way to maximize the statistical confidence is to use generalizable metrics that capture the behavior of as many of the simulated oligomers as possible. Methods based on graph theory have had success in doing this for the modelling of charge transport (29, 30) and the microstructure in bulk heterojunctions (31–33). Enhanced sampling coupled with weighted-histogram analysis can be used to calculate the statistical certainty of an observed state in MD, and metadynamics in particular is often used to great effect in studies on biological systems (34). A third challenge is the requirement for a well-validated force field that is able to capture the unique morphological behaviors of pi-conjugated systems (35). We address these challenges by using enhanced sampling methods, graph theory, and a force field that has previously reproduced many structural features for similar systems (14).

To understand the impact of exchanging glycol side chains for alkyl side chains on the morphology and swelling behavior of mixed transporting polymers, we synthesize a random glycol:alkyl copolymer series (x-p(gT2):y-p(aT2)) by copolymerizing the repeat units of the two hole-transporting ("p-type") polymers: poly(3,3′dialkoxy-(triethyleneglycol)-bithiophene) (p(gT2)) and poly(3,3′ditetradecoxy-bithiophene) (p(aT2)). Thiophene repeat units are chosen because polythiophenes, with their low oxidation potential and good hole transport, are the most commonly studied p-type mixed transport polymer. Thiophene units are also common in many n-type mixed transport systems (10, 11). We vary the ratio of gT2 and aT2 repeat units from 100:0 ("P100"), through 90:10 ("P90"), 75:25 ("P75"), 50:50 ("P50") and 0:100 ("P0", see Fig. 1A for chemical structures), noting that the aT2 repeat units have slightly longer side chains than the gT2 repeat units (tetradecyl compared to triethylene glycol). We experimentally
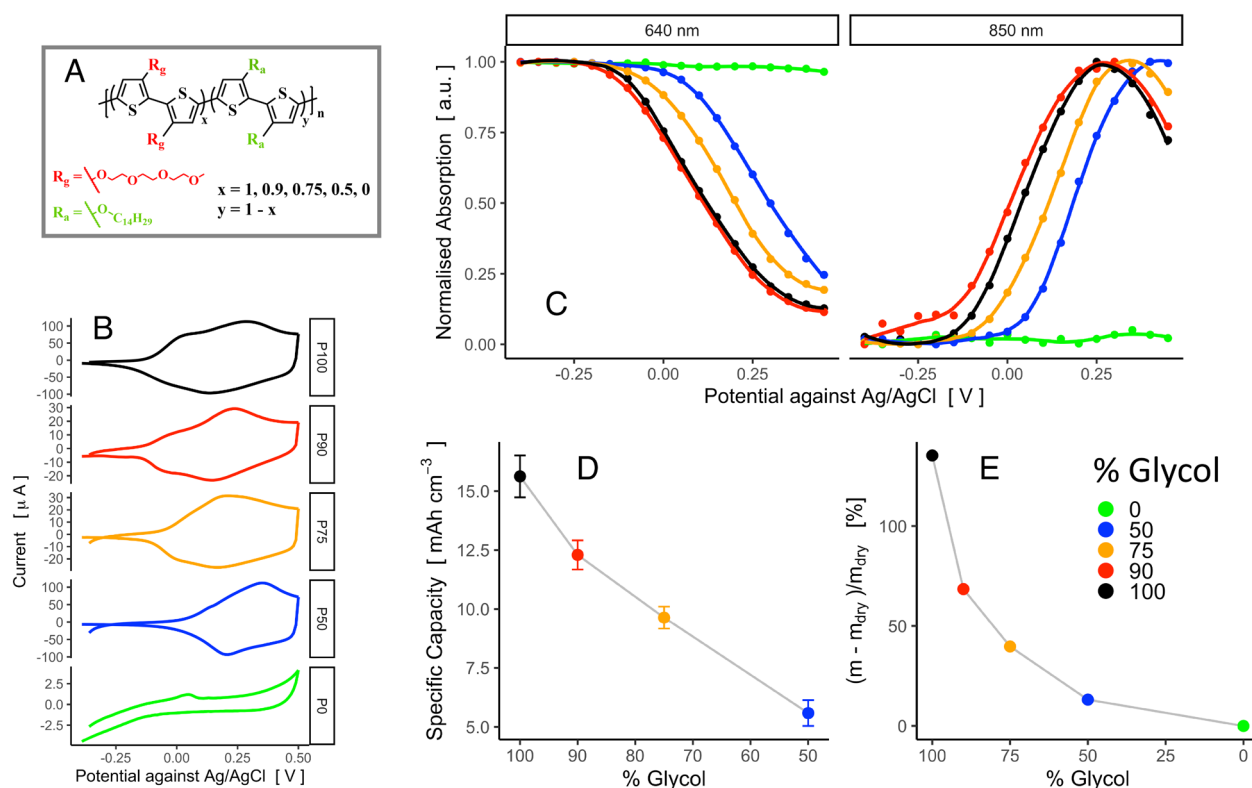


**Fig. 1.** (A) Chemical structure of the *x*-p(gT2):*y*-p(aT2) polymer series with decreasing fraction of triethylene glycol (TEG) side chains and increasing fraction of alkoxy side chains. (B) Thin film CV of the polymer series on ITO glass substrates in Ar-saturated 0.1 M NaCl (aq.) electrolytes with a scan rate of 50 mV/s. (C) Normalized absorbance change of the polymer series at 640 nm (*Left*, neutral state) and 900 nm (*Right*, polaronic state) against the bias applied to the polymer thin films. (D) Volumetric specific capacity of the polymer series at a C-rate of 1,000. The data were interpolated at a *C*-rate value of 1,000, after fitting a log function to the capacitance data shown in *SI Appendix*, Fig. S6. (E) Normalized mass change of the polymer thin films when applied 0.5 V vs. Ag/AgCl for 120 s on the polymer-coated EQCM substrates in Ar-saturated 0.1 M NaCl (aq.) electrolytes.

characterize the copolymer's electrochemical and spectroelectro-chemical properties, their changes in morphology upon wetting and their swelling properties. Experimentally we find a significant reduction in swelling with an increased alkyl fraction, particularly when substituting just 10% of the gT2 units for aT2. The reduction in polymer swelling is accompanied by an increase in its electrochemical stability, i.e., the ability to maintain the redox current intensity over multiple CV scans.

To investigate the amorphous packing of these materials and understand the mechanisms behind the inhibited swelling and increased electrochemical stability, we simulate amorphous assemblies of the polymers using MD and metadynamics. We use analysis based on graph theory to identify polymer networks mediated by contacts between different chemical groups. We then proceed to simulate films of these polymers in water and observe the response of the networks. We find that the networks mediated by alkyl side-chain contacts strengthen upon exposure to water, counteracting the volumetric expansion of the film. Metadynamics simulations reveal that the free energy of aggregation between two partially alkylated polymer segments is significantly stronger than for fully glycolated chain segments, with the difference arising predominantly due to the strong reduction in free energy associated with alkyl side chain aggregation when in a polar environment.

## Methods

**Material Synthesis and Experimental Methods.** The gT2 and aT2 units were copolymerized in ratios of 100:0 (P100), 90:10 (P90), 75:25 (P75), 50:50 (P50) and 0:100 (P0). Detailed synthetic procedures are listed in the *Material Synthesis* of *SI Appendix*. The electrochemical, spectroelectrochemical, and electrogravimetric properties, and microstructural change upon wetting and under electrochemical biases of these materials were characterized using cyclic voltammetry (CV), operando ultraviolet visible spectroscopy (UV-VIS), electrochemical quartz crystal microbalance (EQCM), and grazing incident wide-angle X-ray spectroscopy (GIWAXS). For detailed experimental methods, see *SI Appendix*.

### Theoretical Models and Methods.
*Atomistic simulations.* To model these systems, we perform atomistic Molecular Dynamics (MD) simulations. In addition to simulating the synthesized polymers, we simulated P80, P20, and P10 with glycol to alkyl ratios of 80:20, 20:80, and 10:90, respectively. P20 and P10 are simulated to gain insight into systems with a minority polar fraction, while P80 is simulated to provide a comparative case for P20 and also as it reflects a side-chain ratio used in other studies (27).

To ensure the random arrangement of alkylated repeat units is captured in simulation, for each member of the copolymer series five individual 20-mers were prepared with the alkyl repeat units arranged in different random orders. Each one of these chains is then equilibrated in water for 30 ns to provide equilibrated chains for subsequent simulations. Following equilibration of oligomers in water, each member of the copolymer series is simulated as an ensemble of 100 chains (20 of each random arrangement) in four ways; 1) In water with the water being steadily removed, allowing the morphological changes at different polymer:water mass ratios to be monitored; 2) As a dry amorphous phase after all the water has been removed, allowing for observation of the solid-state morphological features; 3) As a dry amorphous phase with all partial charges set to neutral to observe the effect of polarity in promoting the morphological features observed in the dry amorphous phase; and 4) Films of the dry amorphous phase from stage (2) placed in contact with water to observe the rate at which water enters the film and its impact on the film morphology.

To investigate if the findings are more generally applicable for mixed conducting polymers, we also performed solvent evaporation MD simulations 1) and MD simulations of the dry amorphous phase 2) on an electron-transporting ("n-type") mixed glycol and alkyl copolymer, x(gNDI-gT2):y(aNDI-gT2) (11) in ratios of 90:10 (nP90) and 80:20 (nP80) gNDI-gT2 to aNDI-gT2 units. This polymer series was chosen because NDI-based n-type semiconductors are well studied in this field (5, 11), and experimentally it has been observed in x(gNDI-gT2):y(aNDI-gT2)

copolymers that continuously reduced swelling occurs as the ratio of gNDI-gT2 to aNDI-gT2 is reduced from 100:0 to 90:10 to 75:25, in a qualitatively similar to the x(gT2):y(aT2) series but with a different dependence on the alkylated to glycolated monomer ratio. Furthermore, x(gNDI-gT2):y(aNDI-gT2) copolymers have a significantly different backbone chemistry from the x(gT2):y(aT2) p-type polymers studied here, allowing us to test whether the microstructural features studied here are common across disparate semiconducting polymers. More detailed information on all MD simulations, including all procedural details, can be found in *SI Appendix*.

*Generalization of polymer microstructure into networks.* To characterize the microstructure of the polymers in the MD simulations, we utilize a methodology based on Graph Theory. We define a time-dependent weighted adjacency matrix, $W(t)$, with elements $A_{ij}(t)$, where $i$ and $j$ refer to individual polymer chains and provide the basis for the matrix. Each element of $W(t)$ is given by

$$A_{ij}(t) = \sum_{a \in i} \sum_{b \in j} S_{ab},$$ [1]

where $a$ and $b$ count over the non-hydrogen atoms in polymers $i$ and $j$ respectively, and $S_{ab}$ is equal to 1 if atoms $a$ and $b$ lie within a cutoff distance (0.4 nm), and 0 otherwise. Each value of $A_{ij}(t)$ represents the number of nearest-neighbor atom pairs between $a$ and $b$, and gives the edge weights of $W(t)$.

We proceed to express $W(t)$ as the sum of time-dependent indexed subgraphs (hereafter referred to as "networks"), where the indices indicate the two chemical groups in which atoms $a$ and $b$ reside. We identify three chemical groups, i) polymer backbones, ii) glycol side chains, and iii) alkyl side chains. In the case of the copolymers, this will give rise to three homonetworks, $W_{aa}(t)$, $W_{bb}(t)$, and $W_{gg}(t)$ describing the interpolymer interactions due to alkyl-to-alkyl, backbone-to-backbone, and glycol-to-glycol contacts, respectively. There are also three distinct heteronetworks (six total, but due to nodes being indistinct then $W_{xy} = W_{yx}$), $W_{ag}(t)$, $W_{bg}(t)$, and $W_{ba}(t)$, which describe networks mediated by contacts between atoms belonging to differing chemical groups. An illustration of the network generalization can be seen in Fig. 2.

To quantify the behavior of these graph networks, we use two dimensionless graph metrics: the mean node degree, $\overline{k}(t)$, and the mean square node centrality, $\overline{g^2}(t)$. The $\overline{k}(t)$ measures how well connected the nodes (or polymers) are in the network, while $\overline{g^2}(t)$ measures how close the network is to the percolation limit. Details on how $\overline{k}(t)$ and $\overline{g^2}(t)$ are calculated can be found in *SI Appendix*.

*Metadynamics.* To characterize the change in free energetics of oligomer-oligomer interactions when exchanging glycol side chains for alkyl, metadynamics simulations are performed on a pair of trimers of the glycolated monomer gT2 (i.e. two gT2-gT2-gT2 trimers) and on a pair of trimers where the alkylated monomer aT2 occupies the central repeat unit (two gT2-aT2-gT2 trimers). Metadynamics is a variant of MD, which enhances the sampling of the system by depositing gaussian-shaped energy kernels in a phase space defined by one or more collective degrees of freedom (CDOFs). We define two CDOFs to bias during our metadynamics simulations: $\sigma$, a measure of the number of heavy atoms between the two trimers that are in proximity to each other, to monitor the intertrimer structure and $\Phi$, a function that counts the number of transdihedrals on the backbones of the two trimers to monitor the intratrimer structure. The free energy landscape is then expressed in terms of other CDOFs using a weighted histogram reweighting procedure (36). Metadynamics attempts to fully explore the energetically relevant phase space of a molecular system. We simulate pairs of trimers as the trimers reproduce the local environment of the side chains while keeping the system (two trimers and the solvent) phase space to a computationally accessible size. More detailed information on simulation methods can be found in *SI Appendix*.

### Experimental Results.

*Electrochemical and spectroelectrochemical properties.* To understand the charging characteristics of this polymer series, we first studied their electrochemical and spectroelectrochemical properties in an aqueous electrolyte. Fig. 1*B* shows the first cycle of cyclic voltammetry (CV) measurements of thin films (~150 nm) of the polymers cycled between −0.4 V and 0.5 V vs. Ag/AgCl in Ar-saturated 0.1 M NaCl (aq.) solutions (See *SI Appendix* for experimental details and *SI Appendix*, Fig. S4 for multiple CV cycles). In the case of the fully alkylated P0, a purely capacitive current-voltage character is observed, assigned to the formation of an
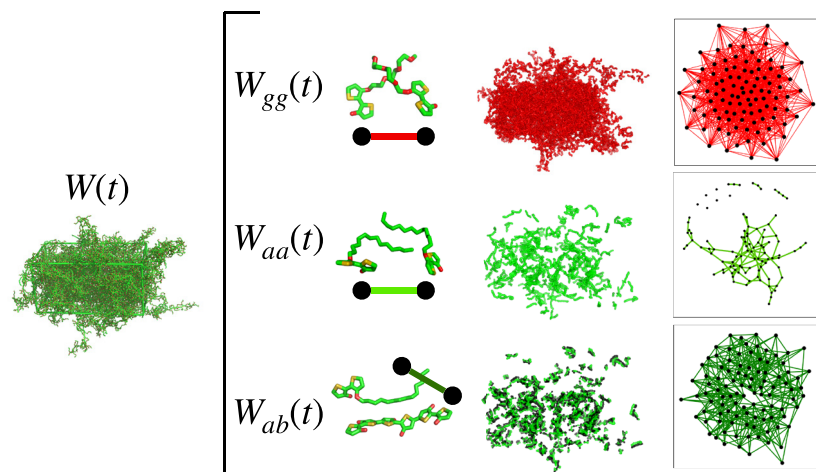
**Fig. 2.** Illustration of the decomposition of an atomistically simulated polymer solid state phase into networks. The first column shows a typical connection that could define a vertex of that network, the middle column shows all of those types of connections present in the polymer film, and the last shows the whole network at a given time.

electrostatic double layer at the material surface. No significant redox features are seen in the CV of P0 when charging the polymer thin films to 0.5 V vs. Ag/AgCl, indicating that the alkyl side chains do not allow ion penetration into the bulk. Among the predominantly glycolated materials, P100 and P90 show similar redox features, including oxidation onsets at $\sim -0.15$ V, the first oxidation peak at $\sim 0$ V and the second at $\sim 0.25$ V. As the fraction of glycol side chains decreases, the intensity of the first oxidation peaks decreases. For P50, the second oxidation peak shifts to higher potential ($\sim 0.35$ V). We tentatively attribute the two oxidation peaks to the formation of hole polarons and bipolarons. However, we note that two distinct peaks can also result from polaron formation in the ordered and disordered regions of the film (25, 37, 38). The decreasing intensity of the first oxidation peak and shifting of the second one can be explained by the decreasing hydrophilicity of the polymer films with decreasing glycol side-chain content. Specifically, lower hydrophilicity leads to, first, a lower equilibrium ion concentration in the passive-swelled polymer thin film, which decreases the first oxidation peak current, and second, a higher difference in anion chemical potential between the electrolyte and the film, which requires a higher bias to drive extra anions into the thin film to compensate holes, i.e. shifts the second oxidation peak to higher biases. Finally, we observe that upon repeated cycling (*SI Appendix*, Fig. S4), while each polymer film shows a reduced current density, P90 sees the smallest loss in the redox peak currents, indicating a higher electrochemical stability than its counterparts. *SI Appendix*, Fig. S7 shows the area under the CV curves for repeated cycling, indicative of the total charge accumulated in the material. In the case of P100, the area decreases under repeated cycling, indicating poor electrochemical stability, while in P90 the total current does not decrease but actually increases slightly upon repeated cycling.

To compare the depth of charging at a certain bias, operando UV-VIS measurements were performed simultaneously with CV. Fig. 1*C* shows the absorption change of the polymer thin films during the first CV oxidation process. Wavelengths of 640 nm and 900 nm correspond to peak absorbance of the polymers in the neutral state and polaronic state, respectively (full spectra are shown in *SI Appendix*, Fig. S5). In line with the electrochemical results, the neutral state absorbance of P0 is nearly unchanged and the polaron absorption band remained absent, meaning P0 is not oxidized. For other polymers, their neutral state absorbance starts to decrease and polaron absorbance starts to increase from a bias of $-0.15$ V, indicating similar oxidation onsets of the four polymers. Upon increasing the bias, the neutral and the polaronic state absorbance of P100 and P90 show similar intensity at the same applied bias, while higher biases are needed to achieve the same change in absorbance in P75 and P50. When charging the polymers over their second oxidation peak potential, the polaron absorbance reduces suggesting that hole polarons convert to bipolarons (37). To investigate the capacitive behavior of these materials, we performed galvanostatic charging/discharging measurements to $+0.5$ V. Due to the different oxidation levels at $+0.5$ V shown by the CV, the polymer series shows monotonically decreasing specific capacities with increasing alkyl side chains (Fig. 1*D*).

***Morphological changes upon wetting and under application of a bias.*** To investigate the effects of passive wetting on the morphology of the films, GIWAXS was performed on P90, P75, and P50 films both before and after exposure to

water for 15 min (see *SI Appendix* for details). When comparing the GIWAXS patterns for the dry copolymer materials with those of P100 and P0 (14) we see the mixed side-chain polymers are overall less crystalline (see *SI Appendix*, Fig. S8 for 2D GIWAXS spectra and *SI Appendix*, Fig. S10 for XRD lineouts), suggesting that the presence of the alkyl chains in a predominantly glycol matrix disturbs the crystalline packing. Upon wetting, all copolymers show a modest reduction in the lamellar stack spacing, which may be attributed to water entering the lamellar stack and leading to an increase in disorder amongst the side chains, causing the side chain end-to-end length to shorten (14).

To investigate the swelling properties of the polymer thin films under electrochemical biases, EQCM measurements are taken on all the synthesized materials in Ar-saturated 0.1 M NaCl (Aq.) (Fig. 1*E*). We see a significant decrease in the degree of swelling between P100 and P90, from 135% to 69% mass change respectively, when switching the bias from $-0.2$ V (slightly before oxidation onset) to 0.5 V vs. Ag/AgCl for 120 s (*SI Appendix*, Fig. S9). Further reduction in swelling is seen for increasing fractions of alkyl side chains, until no appreciable swelling is observed for P0. For all polymers with 75% or more glycol side chains, gain in mass during the oxidation process is preceded by mass loss (*SI Appendix*, Fig. S9). Since this behavior occurs reproducibly over several cycles, we attribute it to the expulsion of cations from the polymer medium prior to anion penetration (39).

To summarize the experimental characterization, the electrochemical and spectroelectrochemical properties of the x(gT2):y(aT2) copolymer series are broadly similar for the purely glycolated polymer and those with a minority fraction of alkyl side chains. However, upon electrochemically biasing the copolymers with alkyl side chains, they show significantly reduced swelling and increased electrochemical stability compared to the purely glycolated polymer, P100. These changes are particularly pronounced when comparing P90 to P100. To investigate why the reduced swelling and increased electrochemical stability occur, we proceed to carry out MD simulations of their amorphous phase.

**Molecular Dynamics Simulations Results.**

***Network formation in the amorphous phase.*** We begin our theoretical work by simulating ensembles of P100, P90, P80, P75, P20, P10, and P0. Each ensemble comprises 100 chains (each containing 20 repeat units), each of which was equilibrated in water for 30 ns before being placed in a $(25 \text{ nm})^3$ simulation cell alongside 200,000 water molecules. The water molecules were removed at a rate of 40,000 molecules every 10 ns until no water was left. The subsequent dry amorphous phase was simulated for a further 100 ns. We monitored the formation and structure of the polymer networks during the removal of the water. The networks are a generalization of the interpolymer structure, where nodes in the network represent polymers in the simulation and edges represent physical contacts between certain chemical groups of the polymers. For example, an edge in a $W_{gg}(t)$ network represents a physical contact between two glycol side chains on different polymers.

At a polymer:water mass ratio of 0.27, the majority of networks in all the materials are already percolating (*SI Appendix*, Fig. S11), the exceptions being for $W_{aa}(t)$ in P90, $W_{gg}(t)$ in P10 and $W_{gg}(t)$ P20. As the water is removed, we see

that a percolating $W_{aa}(t)$ network in P90 forms 50 ns into the simulation (Fig. 3), at a polymer:water mass ratio of 1.35. Interestingly, in P10 the minority network $W_{gg}(t)$ does not form a fully percolating network, even when all solvent has been removed. Instead, it enters a state of transient percolation whereby the network oscillates around the percolation limit (*SI Appendix*, Fig. S13). Aside from $W_{gg}(t)$ in P10, all networks percolate in the dry polymer phase (*SI Appendix*, Fig. S12). Broadly, this can be attributed to the large molecular surface area/volume ratio of a polymer, allowing it to contact many other polymers. The effect of having high molecular area/volume ratio is particularly dominant if the chemical groups involved in the network connections are present in large quantities, for example $W_{gg}(t)$ in P100. However, in cases where the chemical groups are only present as a small fraction of the mass of the material (for example $W_{aa}(t)$ in P90, where the alkyl side chains only represent 8% of the systems mass), then the observation that the alkyl side chains link up sufficiently to form a percolating network is unexpected when considering the statistical likelihood of them doing so in the absence of enthalpic interactions. It is noteworthy that the ratio of 90:10 glycol to alkyl side chains is both the ratio at which the percolating $W_{aa}(t)$ forms as well as the ratio at which we experimentally see a distinct drop in the materials' tendency to swell during electrochemical biasing (Fig. 1*E*).

To understand whether the network formation is a general phenomenon to conjugated glycol:alkyl copolymers, we simulate two n-type polymers, nP90 and nP80, whose backbones comprise alternating NDI and gT2 (triethylene glycol) groups, and the side chains on the NDI unit are either alkyl (octyl, decyl) or glycol (heptakis ethylene glycol) (see *SI Appendix*, Fig. S14*A* for chemical formula). It has been reported that inhibited swelling in these materials does not occur at a glycol:alkyl unit ratio of 90:10, but does at a ratio of 75:25 (11). We observe that a percolating $W_{aa}(t)$ network is not present in nP90, however in nP80 the $W_{aa}(t)$ network shows transient percolation characteristics. Given that these observations are made at a glycol:alkyl unit ratio of 80:20, that connectivities of these networks are likely underestimates due to connections being lost at the simulation cell boundaries and the limited time the networks have to form in simulation, we expect that at a glycol:alkyl ratio of 75:25 there is a percolating $W_{aa}(t)$ network

present in the amorphous phase of this polymer system. We have thus correlated the formation of percolating $W_{aa}(t)$ networks and inhibited swelling in two disparate conducting polymer materials.

***Role of environment in network connectivity.*** For the p-type materials (P100 to P0), we proceed to simulate the dry amorphous phase with all partial charges set to neutral. By comparing the response of the networks with and without partial charges we can directly probe the role of enthalpic interactions in the free energy of the networks (entropy is unaffected by the removal of partial charges). Upon removing partial charges from the simulations, our first observation is that networks mediated by groups that are in a minority by mass fall significantly in their average node connectivity (*SI Appendix*, Fig. S15). This is most notable for the $W_{aa}(t)$ network in P90 and $W_{gg}(t)$ in P10, which lose 40% and 60% of their interpolymer contacts, respectively. Interestingly we also note that the % drop in network connectivity (*SI Appendix*, Fig. S16) for the $W_{aa}(t)$ and $W_{gg}(t)$ networks decrease monotonically with the amount of alkyl side chain (in the case of $W_{aa}(t)$) or glycol side chain (in the case of $W_{gg}(t)$) present in the material. If we consider a single alkyl side chain in a glycol:alkyl copolymer then, the more that side chain is in isolation (i.e., the lower the fraction of alkyl side chains in the material), the bigger the role the partial charges in the side-chain environment appear to have in driving the alkyl side chains to connect together. The parallel effect is true for a single glycol side chain where the more the glycol side chain is in isolation (i.e., the higher the alkyl fraction), the greater the role that its own partial charges have in driving it to connect with other glycol side chains. Due to these observations, we posit that the enthalpic driving forces causing the network edges to form are driven by the difference between the polarity of the side chains and the polarity of their environment.

***Effect of water exposure on networks.*** With the effect of side-chain environment in mind, we proceed to simulate films of the p-type materials in water, calculate the rate at which the films swell when passively exposed to water, and observe the effect of the water on the networks. The films are obtained by taking the dry amorphous phase topologies and expanding the $Z$ axis of the simulation cell to accommodate between 30,000 and 40,000 water molecules
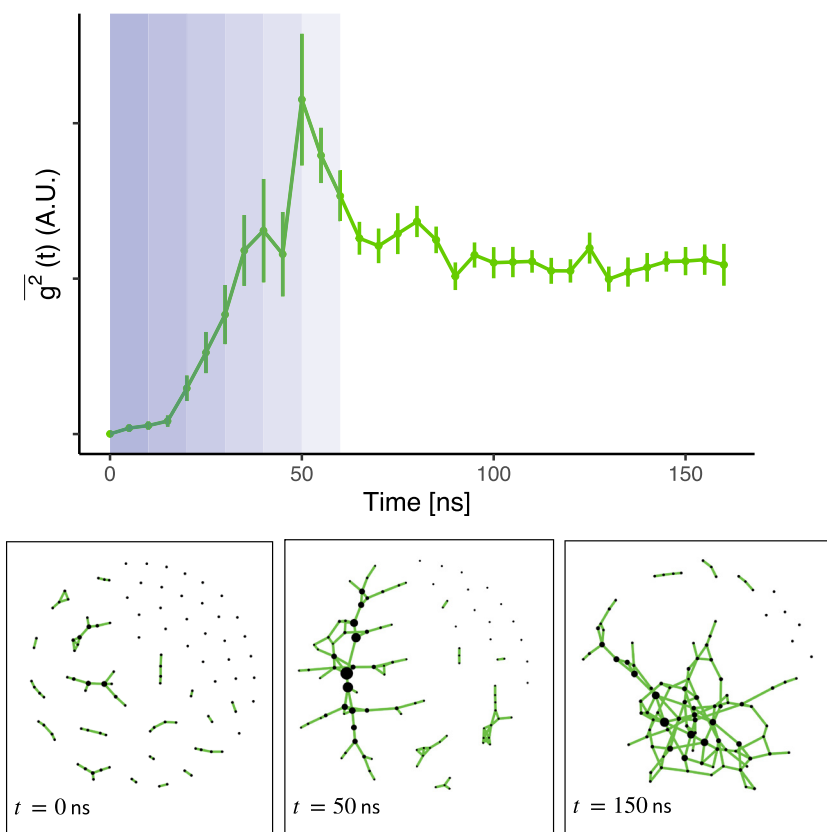


**Fig. 3.**   Mean square centrality for $W_{aa}(t)$ in P90 during the solvent evaporation (indicated in blue between 0 and 60 ns), and in the solid state of the amorphous phase, with a white background between 60 ns and 160 ns. Illustrations of the $W_{aa}(t)$ in P90 networks before the percolation limit (0 ns), at the percolation limit (50 ns) and after surpassing the percolation limit (150 ns). Nodes sized according to their centrality.

in addition to the polymer assembly. When considering the periodicity of the system, the subsequent topologies resemble films approximately 11nm thick, with layers of water about 10nm thick between them. These topologies are simulated for 1.2 μs.

We quantify the rate of mass change of the polymer films in simulation by defining a boundary between the film and the solvent. At each time in the simulation, we calculate the total mass (polymer and water) inside the film boundaries (*SI Appendix*). While the changes in film thickness and mass of the films is small over the 1.2-μs simulations (just 0.8-nm change in thickness for P100), it is sufficient to determine a rate of change of mass. Our initial observation is that the trend in the rate of change of mass (shown in Fig. 4A) closely resembles the experimentally measured mass change under bias. In simulation we see a 50% decrease in rate of mass change from $(2.2 \pm 0.1) \times 10^{-8} \, \mu g \, \mu m^{-2} \, \mu s^{-1}$ to $(1.1 \pm 0.1) \times 10^{-8} \, \mu g \, \mu m^{-2} \, \mu s^{-1}$ when comparing P100 and P90, with the rate of mass change decreasing for higher alkyl contents. P75 is an outlier to the trend, showing a larger rate of mass gain than P80. The deviation from the trend for P75 may be due to a particular surface morphology arising from the poor sampling of the phase space of MD, or error arising from not sufficiently sampling the randomness of the distribution of alkylated and glycolated units. When looking at the simulations of the films in water by eye, the alkyl side chains in P90 are noticeably more clustered after the 1.2 μs simulation compared to before (Fig. 4B).

Upon following the network connectivities for these films, interesting dynamics are observed (demonstrated in Fig. 4C for P90). In all the films containing alkyl side chains, the networks involving alkyl side chains (except for the $W_{ga}(t)$ networks) increase in their average node degree, while those involving glycol side-chain contacts decrease in their average node degree (*SI Appendix*, Fig. S17).

The behavior of the networks involving glycol side chains is consistent with water entering the glycolated regions of the amorphous films and creating a solvation shell around the glycol side chains, inhibiting contact between them and with other chemical groups. In doing so, the polarity of the environment in which the alkyl side chains reside is increased due to water having a higher dielectric constant than glycol side chains (40, 41). As we have seen in the simulations with partial charges removed, reducing the polarity of an alkyl side chain's environment has the effect of weakening the $W_{aa}(t)$ and $W_{ab}(t)$ networks. It is natural then to observe that the ingress of water into the glycolated phase has the opposite effect – it increases the polarity of the alkyl side chain's environment, driving the alkyl side chains to aggregate and subsequently strengthening the $W_{aa}(t)$ and $W_{ab}(t)$ networks.

***Free energetics of polymer interactions.*** To quantify the oligomer and side-chain interactions, metadynamics simulations are performed on either two gT2-gT2-gT2 trimers or two gT2-aT2-gT2 trimers in water, the result of which can be seen in Fig. 5. Fig. 5A shows the free energy of the systems as a function of the intertrimer separation, measured from their geometric centers. We see that the two fully glycolated trimers will aggregate with a free energy of $(-29.1 \pm 0.1)$ kJ/mol, while the two partially alkylated trimers will aggregate with a free energy of $(-47.3 \pm 0.3)$ kJ/mol, as shown in Fig. 5A. These values reflect the observations that both P100 and P90 are insoluble in water when in the neutral state, and that P90 experiences less passive and active swelling than P100.

To understand the impact of exchanging glycol side chains for alkyl side chains on the interoligomer structure, we monitor the fraction of states in our metadynamics simulations with the two trimer backbones in contact and the fraction of states observed with the side chains on the central monomer in contact, as shown in Fig. 5B. In the case of the partially alkylated trimers, we see that $(97.6 \pm 0.1)\%$
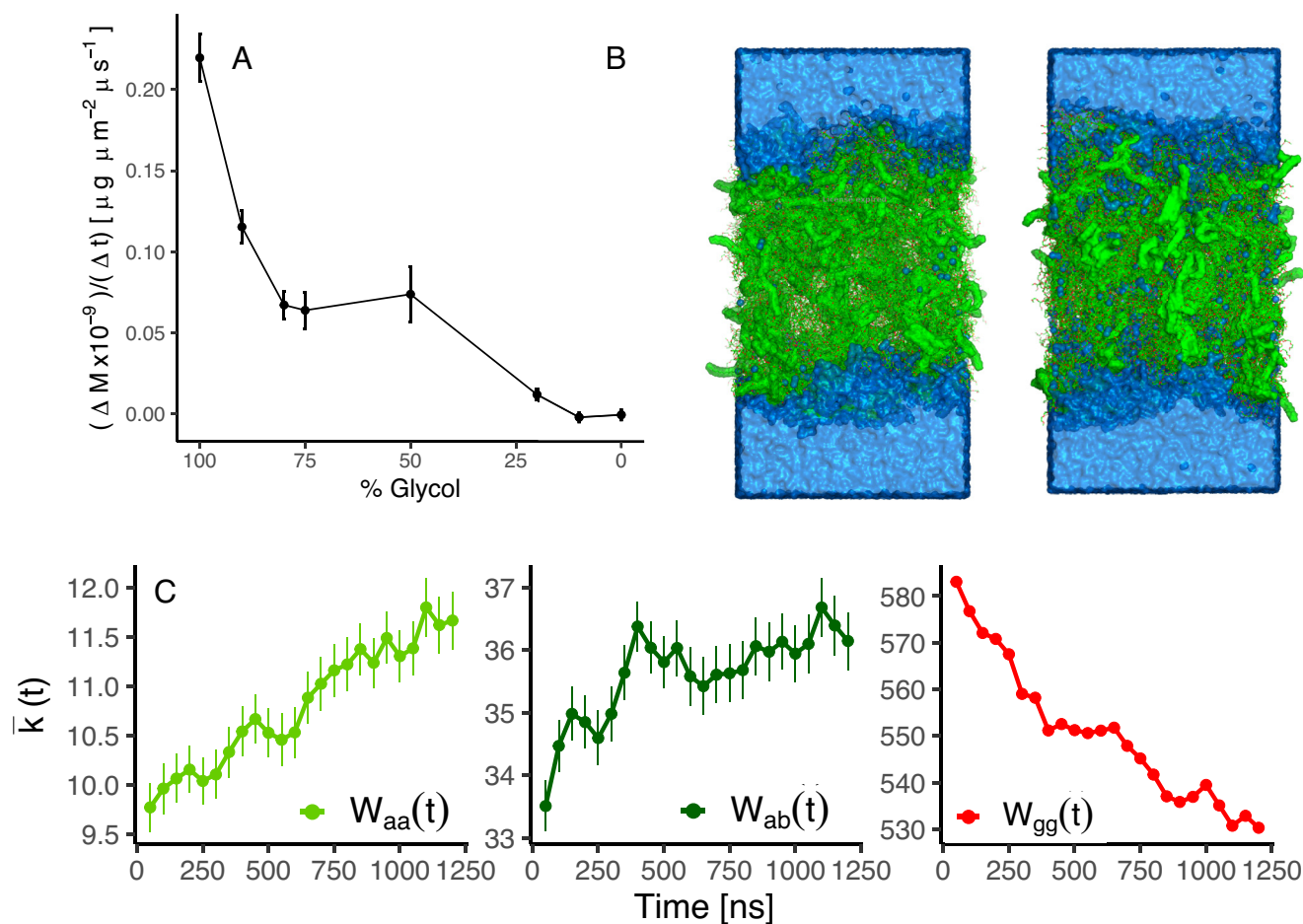


**Fig. 4.** Characterization of the film expansion for the simulated materials. (*A*) Rate of change of mass of the films after exposure to water, (*B*) Illustration of the P90 film immediately after exposure to water, and after 1.2 μs of water exposure. (*C*) The change in the average node degree during the 1.2 μs simulation for $W_{aa}(t)$, $W_{ab}(t)$, and $W_{gg}(t)$, showing the water entering the film and disrupting the glycol–glycol contacts, while the alkyl–alkyl and alkyl–backbone contacts strengthen.
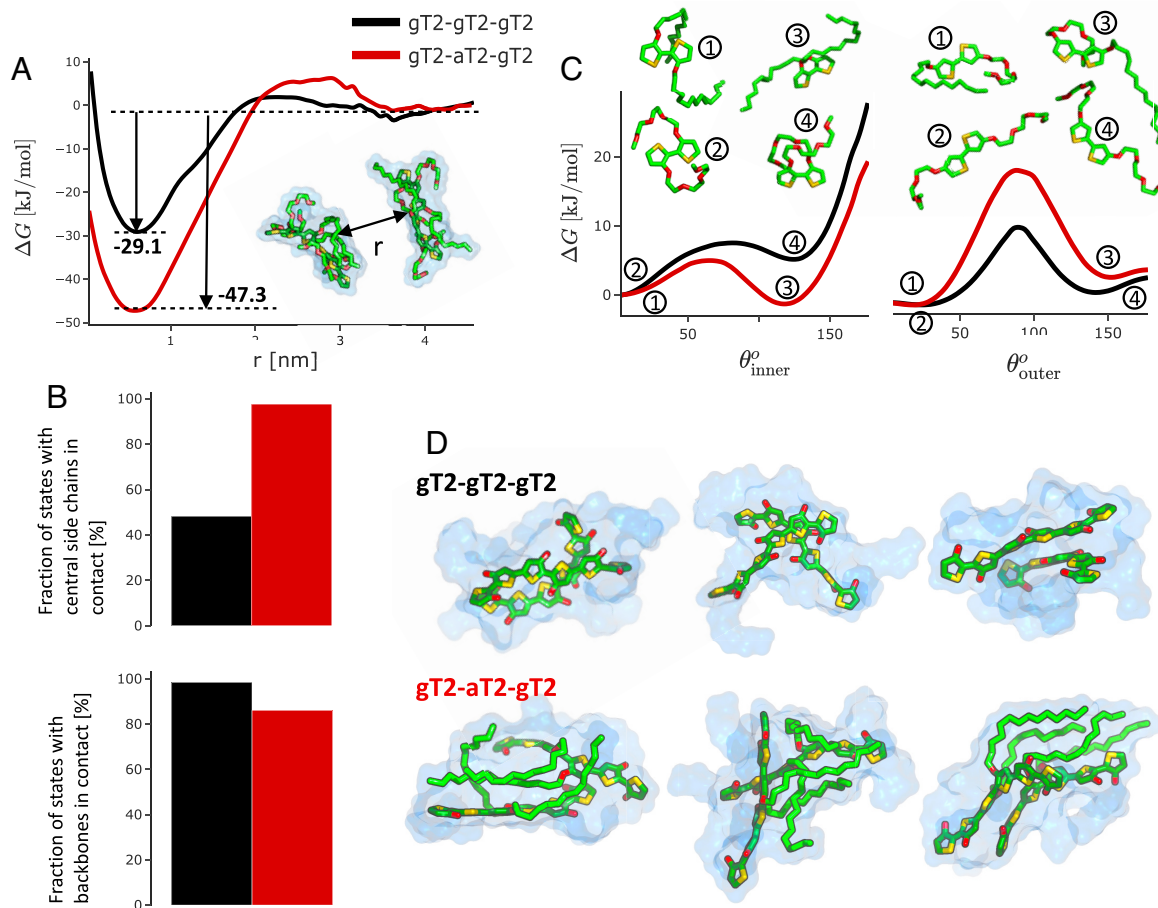
**Fig. 5.** Free energy characterization of the interaction between two trimers either with all glycol side chains, or with the central repeat unit functionalized with alkyl side chains. (*A*) The FES as a function of the distance between the geometric centers of the oligomers, (*B*) the fraction of states for each oligomer pair where the side chains on the central oligomer are in contact with each other (*Top*) or the backbones on the two oligomers are in contact with each other (*Bottom*), (*C*) the FES for the inner and outer dihedrals of the oligomer with examples of the dihedral structures at different points on the FES and (*D*) a sample of low energy states for each of the oligomer pairs. Glycol side chains not shown for clarity but indicated with their solvent accessible surface area in blue.

of the bound states between the two oligomers have their alkyl side chains in contact, with an overall free energy associated with alkyl–alkyl side-chain contact in these systems of $(-11.6 \pm 0.7)$ kJ/mol as shown in *SI Appendix*, Fig. S22. When we compare this to the population of states with the equivalent glycolated side chains in contact, we see only $(48.2 \pm 0.1)\%$ of the states have those side chains in contact, indicating a free energy of $(0.17 \pm 0.02)$ kJ/mol associated with glycol side chains making contact. Interestingly, we also see that the partially alkylated trimers have fewer states with their backbones in contact compared to the glycolated trimers $[(85.9 \pm 0.1)\%$ and $(98.2 \pm 0.1)\%]$, suggesting that the alkyl side chains have the effect of partially blocking backbone–backbone contact. This likely occurs as the alkyl side chains will aggregate with the apolar backbones to avoid the polar water, but also the alkyl side chains are longer than the glycol side chains (14 nonhydrogen atoms compared to 11 for the glycol side chains), meaning they have a larger excluded volume.

When observing the effect on the intraoligomer torsions (Fig. 5*C*) we see primarily that exchanging the central glycol side chains for alkyl side chains has the effect of stabilizing the cis configuration of the inner dihedral (the dihedral between the head-to-head side chains), while the outer dihedral (the dihedral between the repeat units) still favors the transconformation but with the free energy barrier associated with switching between cis and trans being significantly increased. Given the following observations, the structures shown in Fig. 5*D* can be considered typical structures for glycolated and partially alkylated polymer segments in an aqueous environment. Both the fully glycolated trimer pair and the partially alkylated trimer pair are characterized by being aggregated. In the case of the partially alkylated trimers, their alkyl side chains are almost always in contact, but also have the effect of twisting the inner dihedral and partially blocking backbone–backbone contact.

## Discussion

The markedly different free energetics of fully and partially glycolated trimers in water reveals differences both in the interchain and intrachain structures for fully glycolated and partially alkylated polymers in an aqueous environment. In partially alkylated polymers, the alkyl side chains experience a free energetic driving force to pair with other hydrophobic groups (such as other alkyl side chains), increasing the free energy of aggregation between the polymers. However, the desire for alkyl side chains to pair with hydrophobic groups also causes them to pack between backbones on neighboring chains (such as the structure seen on the left in Fig. 5*D*). This may explain why we observe a reduced $\bar{k}(t)$ in the $W_{bb}(t)$ network in P90 compared to in P100 (*SI Appendix*, Fig. S17), and why partially alkylating polythiophenes have been reported to be detrimental for charge transport (27). Furthermore, we observe a switch from a planar trans dihedral to a nonplanar dihedral when exchanging two head-to-head glycol side chains for alkyl side chains. This is most likely so as to bring the two head-to-head alkyl side chains into close proximity with each other, reducing their interface with the water. The free energy associated with the self-aggregation of the head-to-head alkyl side chains on a T2 unit is evidently enough to overcome the backbone planarizing potentials arising from placing oxygen atoms at the side chain attachment point (42).

The behavior of glycolated and partially alkylated trimers in water is consistent with the formation of highly connected $W_{aa}(t)$

and $W_{ab}(t)$ networks in P90 in the solid state, as observed in our MD calculations. This may be expected since P90 presents a relatively polar effective medium to the alkyl chains. The tendency of alkyl side chains to aggregate in the solid state, as well as the observation that the polymers form a percolating network due to subsequently aggregated alkyl side chains, means we can consider the partially alkylated materials as being physically cross-linked. Such physical cross-linking has been observed in biopolymers such as alginates (43), collagen (44), gelatine (45), and agar (46), where the physical cross-links occur due to strong ionic interactions. The behavior seen here for majority glycol copolymers, where apolar units connect within a polar matrix, is more akin to the behavior of mesoscale structures such as vesicles and micelles (47). In hydrogels, physical cross-links with have been correlated with self-healing properties (48, 49) leading to so called "smart gels." In such systems, the physical cross-links have low energy barriers to formation meaning that, when broken, they can readily reform on relevant time scales. We see the same qualitative behavior with alkyl–alkyl aggregation in a polar medium—they have a strong negative free energy of formation with a low energy barrier to formation of (4.8 ± 0.2) kJ/mol as shown in *SI Appendix*, Fig. S22.

The network behaviors observed here can be considered as a balancing of the enthalpic ($\Delta H$) and entropic ($\Delta S$) contributions to the free energy associated with interpolymer contacts ($\Delta G$) in each of the networks according to

$$\Delta G = \Delta H - T\Delta S,$$

where $T$ is the temperature. During the solvent evaporation procedure (for example $W_{aa}(t)$ formation shown in Fig. 3) the networks form as $-T\Delta S$ becomes progressively more negative. The increase in entropy associated with edge formation during solvent evaporation occurs primarily due to the reducing volume of space in which the polymers reside and the increasing proximity of alkyl side chains as the water is removed. Alternatively, one can consider the increase in entropy of edge formation during the solvent evaporation to be a result of the total fraction of microstates associated with an edge increasing as the water is removed and the polymers come into closer proximity.

In the dry solid state, if the alkyl side chains are in the minority $\Delta H$ is very negative for a $W_{aa}(t)$ network due to the significantly different polarity of the alkyl side chains and their environment (mostly polar glycol side chains). When alkyl side chains are in the majority, $-T\Delta S$ is very negative due to most microstates having alkyl side chains in contact. Therefore, the observation that these networks tend to percolate at all alkyl fractions is explained by the networks being enthalpically driven at one extreme when the mediating chemical group is in the minority (for example $W_{aa}(t)$ in P90), and entropically driven at the other when it is in the majority (for example $W_{aa}(t)$ in P10).

Swelling, on the other hand, has the effect of increasing the overall polarity of the bulk, while also applying a separating force on the physical cross-links as the material expands to accommodate the ingress of water and ions. Both of these effects will depend on the level of electrolyte penetration into the polymer phase. We further note that given the ions do not significantly affect the polarity of the aqueous electrolyte, nor preclude the penetration of water into the bulk, the observations made for films in water are likely to hold upon the use of electrolytes with different ions and ion concentrations.

Whether the film holds or loses its structural integrity will be a balance between the following considerations: Is there a sufficient quantity of apolar side chains such that a percolating network can form in the solid state? If so, will those contacts be strong enough, or strengthen enough in response to electrolyte ingress, so as to be able to counteract the potential associated with excessive swelling? The final consideration need also apply under the electrochemical doping of the polymers. Given that excess charges on electrochemically doped polymers reside on the backbones, which do not participate in the $W_{aa}(t)$ network, the formation of $W_{aa}(t)$ will likely still occur when the polymer is electrochemically doped. However, the electrochemical doping will increase the ingress of electrolyte, influencing the balance of forces (interpolymer, polymer-electrolyte) for any given alkyl:glycol side-chain ratio. The point at which the structural resilience is obtained using copolymers as discussed here will depend on several factors including backbone chemistry, the length, and structure of side chains, as well as fraction of alkylated monomers. The experimental and simulated results here and in literature show that for polythiophenes such as these, as well as some n-types such as gNDI-T2 (11), the balance is struck for polymers with 10% or more alkyl side chains. For some n-types such as gNDI-gT2, 25% or more alkyl side chains are required to form resilient $W_{aa}(t)$ networks (11).

## Conclusion

In this study we have synthesized, characterized, and modeled a series of mixed transport polymers based on the archetypal p-type polymer p(g3T2). In the series, we alter the ratio of glycol side chains to alkyl side chains to improve the materials' electrochemical stability. We experimentally characterized the materials and find that upon exchanging 10% of the glycol side chains for alkyl the swelling of the material is much reduced, the electrochemical stability is significantly improved, and the charging/discharging characteristics are mostly unchanged.

Upon modeling these materials, we have found that alkyl side chains have a strong tendency to aggregate when in a polar environment, resulting in the formation of alkyl–alkyl physical cross-links between polymers. The alkyl–alkyl physical cross-links allow for the formation of a supramolecular polymer network that is resistant to water ingress into the bulk, resulting in reduced swelling and the preservation of the film microstructure. Metadynamics results highlight the strength of these physical cross-links, while also suggesting that the alkyl side chains can lead to local changes to the polymer backbone that may be detrimental for electronic charge transport. As well as correlating the presence of this network to the reduced tendency to swell in these archetypal p-types, we have shown that the same relationship applies in an n-type polymer series of different backbone structure.

To maximize the number of physical cross-links that each polymer can form it would be desirable to synthesize polymers with high molecular weights. Furthermore, to maximize the interaction between alkyl side chains between polymers it would be desirable to use long, non-branched alkyl side chains, as we do in this study. Additionally, to maximize the strength of the physical cross-links, chemical designs could be applied to maximize the difference in the polarity of the mediating side chains and its environment. As many of the results found for alkyl side chains in a predominantly polar material shows analogous behavior when considering glycol side chains in a predominantly apolar material, the same design principles could be used for copolymers with majority alkyl side chains and an apolar electrolyte. A further direction for future study is the impact of side chain–induced changes in backbone conformation or connectivity on electronic transport properties. Identification of such microstructural features, the driving forces behind their formation, and their impacts on functional properties, will continue to help towards the development of stable mixed transport electronic devices.

Author affiliations: [a]Department of Physics, Imperial College, London, South Kensington, London SW7 2AZ, United Kingdom; [b]Department of Materials Science and Engineering, Stanford University, Stanford, CA 94305; [c]King Abdullah University of Science and Technology Solar Center, Division of Physical Sciences and Engineering, King Abdullah University of Science and Technology, Thuwal 23955, Saudi Arabia; [d]Department of Chemistry and Chemical Engineering, Chalmers University of Technology, Göteborg 412 96, Sweden; and [e]Department of Chemistry, Imperial College, London, South Kensington, London SW7 2AZ, United Kingdom

1. K. A. Ludwig, J. D. Uram, J. Yang, D. C. Martin, D. R. Kipke, Chronic neural recordings using silicon microelectrode arrays electrochemically deposited with a poly(3,4-ethylenedioxythiophene) (PEDOT) film. *J. Neural. Eng.* **3**, 59–70 (2006).
2. L. R. Savagian *et al.*, Balancing charge storage and mobility in an oligo(ether) functionalized dioxythiophene copolymer for organic- and aqueous- based electrochemical devices and transistors. *Adv. Mater.* **30**, e2004250 (2018).
3. A. Giovannitti *et al.*, The role of the side chain on the performance of N-type conjugated polymers in aqueous electrolytes. *Chem. Mater.* **30**, 2945–2953 (2018).
4. A. Giovannitti *et al.*, Controlling the mode of operation of organic transistors through side-chain engineering. *Proc. Natl. Acad. Sci. U.S.A.* **113**, 12017–12022 (2016).
5. D. Moia *et al.*, Design and evaluation of conjugated polymers with polar side chains as electrode materials for electrochemical energy storage in aqueous electrolytes. *Energy Environ. Sci.* **12**, 1349–1357 (2019).
6. J. Gladisch *et al.*, Reversible electronic solid-gel switching of a conjugated polymer. *Adv. Sci.* **7**, 1901144 (2019).
7. M. Moser *et al.*, Side chain redistribution as a strategy to boost organic electrochemical transistor performance and stability. *Adv. Mater.* **2002748**, 1–6 (2020).
8. M. Moser *et al.*, Ethylene glycol-based side chain length engineering in polythiophenes and its impact on organic electrochemical transistor performance. *Chem. Mater.* **32**, 6618–6628 (2020).
9. P. Schmode *et al.*, The key role of side chain linkage in structure formation and mixed conduction of ethylene glycol substituted polythiophenes. *ACS Appl. Mater. Interfaces* **11**, 13029–13039 (2020).
10. I. P. Maria *et al.*, The effect of alkyl spacers on the mixed ionic-electronic conduction properties of N-type polymers. *Adv. Funct. Mater.* **31**, 2008718 (2021).
11. A. A. Szumska *et al.*, Reversible electrochemical charging of n-type conjugated polymer electrodes in aqueous electrolytes. *J. Am. Chem. Soc.* **143**, 14795–14805 (2021).
12. D. Ohayon *et al.*, Biofuel powered glucose detection in bodily fluids with an n-type conjugated polymer. *Nat. Mater.* **19**, 456–463 (2020).
13. A. Maria Pappa *et al.*, Direct metabolite detection with an n-type accumulation mode organic electrochemical transistor. *Sci. Adv.* **4**, eaat0911 (2018).
14. N. Siemons *et al.*, Impact of side-chain hydrophilicity on packing, swelling, and ion interactions in oxy-bithiophene semiconductors. *Adv. Mater.* **39**, 2204258 (2022).
15. S. Moro *et al.*, The effect of glycol side chains on the assembly and microstructure of conjugated polymers. *ACS Nano* **16**, 21303–21314 (2022).
16. E. Tan *et al.*, The role of long-alkyl-group spacers in glycolated copolymers for high-performance organic electrochemical transistors. *Adv. Mater.* **34**, e2202574 (2022).
17. S. E. Chen *et al.*, Impact of varying side chain structure on organic electrochemical transistor performance: A series of oligoethylene glycol-substituted polythiophenes. *J. Mater. Chem. A Mater.* **19**, 10738–10749 (2022).
18. D. J. Woods *et al.*, Side-chain tuning in conjugated polymer photocatalysts for improved hydrogen production from water. *Energy Environ. Sci.* **13**, 1843–1855 (2020).
19. S. A. J. Hillman *et al.*, Why do sulfone-containing polymer photocatalysts work so well for sacrificial hydrogen evolution from water? *J. Am. Chem. Soc.* **144**, 19382–19395 (2022).
20. S. Cong *et al.*, Tunable control of the hydrophilicity and wettability of conjugated polymers by a postpolymerization modification approach. *Macromol. Biosci.* **20**, 2000087 (2020).
21. P. Schmode *et al.*, The key role of side chain linkage in structure formation and mixed conduction of ethylene glycol substituted polythiophenes. *ACS Appl. Mater Interfaces* **12**, 13029–13039 (2020).
22. B. Meng *et al.*, Replacing alkyl with oligo(ethylene glycol) as side chains of conjugated polymers for close π-π stacking. *Macromolecules* **48**, 4357–4363 (2015).
23. X. Chen, Z. Zhang, Z. Ding, J. Liu, L. Wang, Diketopyrrolopyrrole-based conjugated polymers bearing branched oligo(ethylene glycol) side chains for photovoltaic devices. *Angew. Chem.* **128**, 10532–10536 (2016).
24. A. Savva *et al.*, Balancing ionic and electronic conduction for high-performance organic electrochemical transistors. *Adv. Funct. Mater.* **1907657**, 1–9 (2020).
25. L. Q. Flagg *et al.*, Polymer crystallinity controls water uptake in glycol side-chain polymer organic electrochemical transistors. *J. Am. Chem. Soc.* **141**, 4345–4354 (2019).
26. R. Giridharagopal *et al.*, Electrochemical strain microscopy probes morphology-induced variations in ion uptake and performance in organic electrochemical transistors. *Nat. Mater.* **16**, 737–742 (2017).
27. A. Khot, B. M. Savoie, How side-chain hydrophilicity modulates morphology and charge transport in mixed conducting polymers. *J. Polymer Sci.* **60**, 610–620 (2022).
28. N. Siemons, Molecular dynamics forcefield. *Github*. https://github.com/nicholas9182/ForceField_for_Conjugated_Polymers. Accessed 1 June 2023.
29. B. M. Savoie *et al.*, Mesoscale molecular network formation in amorphous organic materials. *Proc. Natl. Acad. Sci. U.S.A.* **111**, 10055–10060 (2014).
30. N. E. Jackson, L. X. Chen, M. A. Ratner, Charge transport network dynamics in molecular aggregates. *Proc. Natl. Acad. Sci. U.S.A.* **113**, 8595–8600 (2016).
31. N. Juneja, J. Zola, V. Chandola, O. Wodo, "Graph-based strategy for establishing morphology similarity" in *33rd International Conference on Scientific and Statistical Database Management* (Association for Computing Machinery, 2021), pp. 169–180.
32. V. Ellen, M. Jones, E. Jankowski, O. Wodo, Using graphs to quantify energetic and structural order in semicrystalline oligothiophene thin films. *Mol. Syst. Des. Eng.* **3**, 853–867 (2018).
33. O. Wodo, S. Tirthapura, S. Chaudhary, B. Ganapathysubramanian, A graph-based formulation for computational characterization of bulk heterojunction morphology. *Org. Electron* **13**, 1105–1113 (2012).
34. S. Furini, C. Domene, Computational studies of transport in ion channels using metadynamics. *Biochim. Biophys. Acta Biomembr.* **1858**, 1733–1740 (2016).
35. K. H. Dubay *et al.*, Accurate force field development for modeling conjugated polymers. *J. Chem. Theory Comput.* **8**, 4556–4569 (2012).
36. D. Branduardi, G. Bussi, M. Parrinello, Metadynamics with adaptive gaussians. *J. Chem. Theory Comput.* **8**, 2247–2254 (2012).
37. C. Enengl *et al.*, Doping-induced absorption bands in P3HT: Polarons and bipolarons. *ChemPhysChem* **17**, 3836–3844 (2016).
38. J. Nightingale, J. Wade, D. Moia, J. Nelson, J. S. Kim, Impact of molecular order on polaron formation in conjugated polymers. *J. Phys. Chem. C* **122**, 29129–29140 (2018).
39. L. Q. Flagg *et al.*, P-type electrochemical doping can occur by cation expulsion in a high-performing polymer for organic electrochemical transistors. *ACS Mater Lett.* **2**, 254–260 (2020).
40. N. Koizumi, T. Hanai, "Dielectric properties of polyethylene glycols: Dielectric relaxation in solid state (special issue on polymer chemistry, I)." in *Bulletin of the Institute for Chemical Research*, (Kyoto University, 1964), vol. **42**, p. 115–127.
41. C. G. Malmberg, A. A. Maryott, Dielectric constant of water from 0 to 100 C. *J. Res. Natl. Inst. Stand. Technol.* **56**, 1–8 (1956).
42. K. J. Thorley, I. McCulloch, Why are S-F and S-O non-covalent interactions stabilising? *J. Mater. Chem. C Mater.* **6**, 12413–12421 (2018).
43. H. Hecht, S. Srebnik, Structural characterization of sodium alginate and calcium alginate. *Biomacromolecules* **17**, 2160–2167 (2016).
44. K. S. Weadock, E. J. Miller, L. D. Bellincampi, J. P. Zawadsky, M. G. Dunnl, Physical crosslinking of collagen fibers: Comparison of ultraviolet irradiation and dehydrothermal treatment. *J. Biomed. Mater. Res.* **29**, 1373–1379 (1995).
45. D. Hellio, M. Djabourov, Physically and chemically crosslinked gelatin gels. *Macromol. Symposia* **241**, 23–27 (2006).
46. X. Li, Q. Yang, Y. Zhao, S. Long, J. Zheng, Dual physically crosslinked double network hydrogels with high toughness and self-healing properties. *Soft Matter* **13**, 911–920 (2017).
47. A. Blanazs, S. P. Armes, A. J. Ryan, Self-assembled block copolymer aggregates: From micelles to vesicles and their biological applications. *Macromol. Rapid Commun.* **30**, 267–277 (2009).
48. Z. Gong *et al.*, High-strength, tough, fatigue resistant, and self-healing hydrogel based on dual physically cross-linked network. *ACS Appl. Mater Interfaces* **8**, 24030–24037 (2016).
49. N. Samadi, M. Sabzi, M. Babaahmadi, Self-healing and tough hydrogels with physically cross-linked triple networks based on Agar/PVA/Graphene. *Int. J. Biol. Macromol.* **107**, 2291–2297 (2018).
50. N. Siemons, Molecular dynamics data. Zenodo. https://doi.org/10.5281/zenodo.8058747. Accessed 1 June 2023.